

Article

An Improved Spatio-Temporally Smoothed Coherence Factor Combined with Delay Multiply and Sum Beamformer

Ziyang Guo ^{1,2}, Xingguang Geng ¹, Fei Yao ¹, Liyuan Liu ^{1,2}, Chaohong Zhang ^{1,2}, Yitao Zhang ^{1,2,*} 
and Yunfeng Wang ^{1,2}

¹ Institute of Microelectronics of Chinese Academy of Sciences, Beijing 100029, China

² University of Chinese Academy of Sciences, Beijing 100049, China

* Correspondence: zhangyitao@ime.ac.cn

Abstract: Delay multiply and sum beamforming (DMAS) is a non-linear method used in ultrasound imaging which offers superior performance to conventional delay and sum beamforming (DAS). While the combination of DMAS and coherence factor (CF) can further improve single plane-wave imaging lateral resolution, by using CF to weight the DMAS output, the main lobe width and aberration effects can be suppressed, which will improve the disadvantage of low lateral resolution when imaging with a single plane-wave. However, in low signal-to-noise ratio (SNR) environments, the speckle variance of the image increases, and there are black area artifacts around high echo objects. To improve the quality of the scatter without significantly reducing the lateral resolution of the DMAS-CF, this paper proposes an adaptive spatio-temporally smoothed coherence factor (GSTS-CF) combined with delay multiply and sum beamformer (DMAS + GSTS-CF), which uses the generalized coherence factor (GCF) as a local coherence detection tool to adaptively determine the subarray length to obtain an improved adaptive spatio-temporally smoothed factor, and uses this factor to weight the output of DMAS. The simulation and experimental data show that the proposed method improves lateral resolution (20 mm depth) by 86.87% compared to DAS, 52.13% compared to DMAS, 15.84% compared to DMAS + STS-CF, and has a full width at half maxima (FWHM) similar to DMAS-CF. The proposed method improves the speckle signal-to-noise ratio (sSNR) by 87.85% (simulation) and 77.84% (in carotid) compared to DMAS-CF, 20.37% (simulation) and 40.74% (in carotid) compared to DMAS, 15.03% (simulation) and 13.46% (in carotid) compared to DMAS + STS-CF, and has sSNR and scatter variance similar to DAS. This indicates that the method improves scatter quality (lower scatter variance and higher sSNR) without significantly reducing lateral resolution.

Keywords: ultrasound imaging; plane-wave; beamforming; coherence factor; adaptive; spatio-temporally smoothed; delay multiply and sum beamforming



Citation: Guo, Z.; Geng, X.; Yao, F.; Liu, L.; Zhang, C.; Zhang, Y.; Wang, Y. An Improved Spatio-Temporally Smoothed Coherence Factor Combined with Delay Multiply and Sum Beamformer. *Electronics* **2023**, *12*, 3902. <https://doi.org/10.3390/electronics12183902>

Academic Editor: Stefano Ricci

Received: 16 August 2023

Revised: 4 September 2023

Accepted: 7 September 2023

Published: 15 September 2023



Copyright: © 2023 by the authors. Licensee MDPI, Basel, Switzerland. This article is an open access article distributed under the terms and conditions of the Creative Commons Attribution (CC BY) license (<https://creativecommons.org/licenses/by/4.0/>).

1. Introduction

In ultrasound imaging, we generally use a fixed focus at emission and a dynamic focus at reception, which allows imaging at frame rates in the tens of Hertz to be obtained [1]; however, this is not suitable for high frame rate imaging such as echocardiography, 3D imaging, and elastography [2,3]. The plane-wave scanning approach achieves high frame rates, but the lack of emission focus severely degrades the imaging quality. Although some traditional coherence factor methods can suppress clutter and improve image contrast with low computational complexity, the ability to reduce scattering variance and remove black-area artefacts is still insufficient, which makes the image background inhomogeneous. Therefore, simultaneously improving the lateral resolution and background scattering quality has become the focus of this research. Based on the spatio-temporally smoothed coherence factor (STS-CF) [4], we propose a new coherence factor method that can adaptively change the length of the smoothing subarray according to the detection target. It provides better side and/or grating lobe suppression, clutter reduction, and aberration correction. To achieve a trade-off between

lateral resolution and scattering retention performance, we combined the new coherence factor with the DMAS method to further improve lateral resolution.

One of the most common beamformers is the delay and sum beamforming (DAS), but its ability to improve image resolution and suppress clutter interference is limited. Giulia Matrone et al. introduced DMAS based on receive aperture autocorrelation, which, unlike DAS, is a non-linear algorithm in which signals are combined and coupled and then multiplied before summing [5]. This means that a correlation operation is conducted on the echoes. Since DMAS multiplies echoes of almost the same frequency, DC and second harmonic components appear in the output spectrum. Therefore, a band-pass filter is added after the DMAS output to filter out DC components and higher harmonic components, while the signal centered at $2f_0$ remains unchanged (f_0 is the central frequency of the echo), and finally the output of the filtered delayed multiplication sum (F-DMAS) is obtained [6]. Compared to DAS, DMAS better suppresses spurious and noise via a correlation operation, brings the measure of backward scattering signal coherence into the beamforming process, and increases the number of new “artificial apertures” (because the coefficient of the autocorrelation function is $2N - 1$ and N is the number of received apertures), thus reducing $f\#$ and resulting in an improvement in lateral resolution [7]. However, this imaging method requires further suppression of the side lobes to improve the imaging quality.

A number of scholars have proposed correcting the output of DMAS with a CF-like method, which can develop for side lobe suppression, clutter reduction, and aberration correction. By adaptively weighting the beamsum, they can enhance image contrast without sacrificing spatial resolution. In addition, they have low computational complexity and are easy to implement. The most representative CF-like method is the coherence factor (CF) [8,9], which is defined as the ratio between the coherent energy of the aperture received signal and the total energy (non-coherent). By using CF to weigh the output of beamforming, the side lobes and aberration effects can be suppressed, but this darkens the image and even reconstructs the image with errors. p.-C. Li and M.-L. Li proposed the generalized coherence factor (GCF), a spatial frequency domain version of CF, which adds a low frequency signal that is not very different from the axial fundamental frequency signal to the molecule of CF and improves the preservation of scatter [10]. Camacho et al. [11] designed the phase coherence factor (PCF) and the sign coherence factor (SCF). The principle is to replace the amplitude information with the phase information, and a linear or exponential relationship curve was added to regulate the suppression of off-axis signals and the retention of background scatter. This suppresses the side lobe and improves the lateral resolution. The implementation of this technique is simple and practical.

Although the CF-like method combined with the DMAS beamformer has advantages, the images may suffer some undesirable effects in a low-SNR environment. They include overall image brightness reduction, increased speckle variance, underestimation of the size of the point target, black area artifacts in the region around the high echo reflector, and even removal of the speckle pattern. To solve the above problems, we introduced and improved the spatio-temporally smoothed coherence factor (STS-CF) proposed by MengLing Xu et al. [12], the essence of which is to measure the coherence between the split subarrays. It uses spatial smoothing (i.e., sub-aperture averaging) to create overlapping subarrays and temporal smoothing across multiple time samples to calculate the energy of the coherence sum [13]. This method introduces a tunable factor, achieving a balance between image quality and algorithmic robustness. However, the value of the subarray length L is determined empirically, and the most appropriate L is different in different environments, so the method performs generally in clinical applications.

To solve the above problem, we propose the GSTS-CF. In this study, we use GCF to detect local coherence and adaptively determine the subarray length for spatial smoothing [14]. Using this factor to weigh the DMAS output can improve the scatter quality without significantly reducing the lateral resolution. This is more applicable in complex clinical settings. Section 2 briefly introduces the framework background of GCF, STS-CF,

and DMAS, and then we describe the proposed method. Section 3 describes the simulation setup and experimental steps and provides some metrics for evaluating a different beamformer. Section 4 shows the obtained images and discusses the results. The performance of these methods and the possibilities for further improvements are discussed in Section 5. Section 6 provides a conclusion of the proposed method of this paper.

2. Materials and Methods

2.1. Spatio-Temporally Smoothed Coherence Factor

In CF, coherence is measured by a single element at a single time metric [15]; the formula of the CF is:

$$CF(p) = \frac{\left| \sum_{m=0}^N x_m(p) \right|^2}{N \sum_{m=0}^N |x_m(p)|^2} \quad (1)$$

where N is the number of elements, and $x_m(p)$ is the delayed signal received by the m -th element at point p . These signals are susceptible to noise and side lobes interference. To make the background region scatter more uniform, the STS-CF is introduced [11]. It divides the array into $N - L + 1$ mutually overlapping subarrays and measures the coherence of the array signal at $2K + 1$ sampling points. It uses the beamsum of the subarrays instead of the single element signal [16]. The mathematical expression is defined as:

$$STS-CF(p) = \frac{\sum_{k=-K}^K \left| \sum_{l=1}^{N-L+1} \sum_{m=l}^{L+l-1} x_m(p+k) \right|^2}{(N-L+1) \sum_{k=-K}^K \sum_{l=1}^{N-L+1} \left| \sum_{m=l}^{L+l-1} x_m(p+k) \right|^2} \quad (2)$$

where L is the length of the subarrays, and $x_m(p+k)$ is the delayed signal received by the m -th element at time index $p+k$. The temporal smoothed technique divides the received array into $N - L + 1$ overlapping subarrays containing L elements and uses the subarray instead of a single element to measure the coherence of the signal. L as an adjustable parameter is able to balance between performance and algorithmic robustness, when $K = 0$ and $L = 0$, STS-CF is CF; when $K = 0$ and $L = M$, $STS - CF \equiv 1$, which means no correction to the beamformer output.

2.2. Generalized Coherence Factor

CF not only suppresses off-axis interference but also filters out useful off-axis signals, which is unstable in a low signal-to-noise ratio environment [14]. The GCF method is based on an improved form of CF. To enhance the robustness, GCF considers the energy of non-coherent scattering signals. It adds low-frequency signals that do not differ much from the axial orientation to the numerator of Equation (1) [15]. It is defined as the ratio of the spectral energy of a particular low-frequency region to the total energy, and its mathematical expression is:

$$GCF(p) = \frac{\sum_{f \in LFR} |h(f, p)|^2}{\sum_{f=0}^{N-1} |h(f, p)|^2} \quad (3)$$

where $h(f, p)$ is the discrete Fourier transform of the delay-compensated aperture data for imaging point p , and the low-frequency region (LFR) is determined by the cutoff frequency M_0 , which determines the performance of the GCF. When $M_0 = 0$, GCF becomes CF.

2.3. Delay Multiply and Sum Beamforming

In DMAS, the signal is delayed, coupled, and multiplied, and then the absolute value of the multiplied couple is square-rooted while preserving the sign, and the resulting signal

is summed and band-pass filtered (BP). If the receiving aperture is N transducers, then there will be $N(N - 1)/2$ combinations. The expression of DMAS is:

$$y_{DMAS}(t) = \sum_{i=1}^{N-1} \sum_{j=i+1}^N \hat{s}_{ij}[t] = \sum_{i=1}^{N-1} \sum_{j=i+1}^N \text{sign}(s_i(t)s_j(t)) \cdot \sqrt{|s_i(t)s_j(t)|} \quad (4)$$

where $s_i(t)$ and $s_j(t)$ are the delayed RF signals received by the i -th and j -th transducer elements, and $\text{sign}(x)$ is the sign function. Due to the multiplication of signals with similar frequencies, a DC and a second harmonic component appear in the spectrum of the DMAS. Therefore, band-pass filtering is further introduced to filter the DC and higher frequency components, and the filtered DMAS is called F-DMAS.

2.4. Proposed Method

We proposed an adaptive spatio-temporally smoothed coherence factor based on GCF, called GSTS-CF, which uses GCF as a local coherence detection tool to determine the subarray length adaptively [13]. To further improve the image sharpness of GSTS-CF, it is combined with the DMAS, which is DMAS + GSTS-CF. The algorithm flowchart is shown in Figure 1.

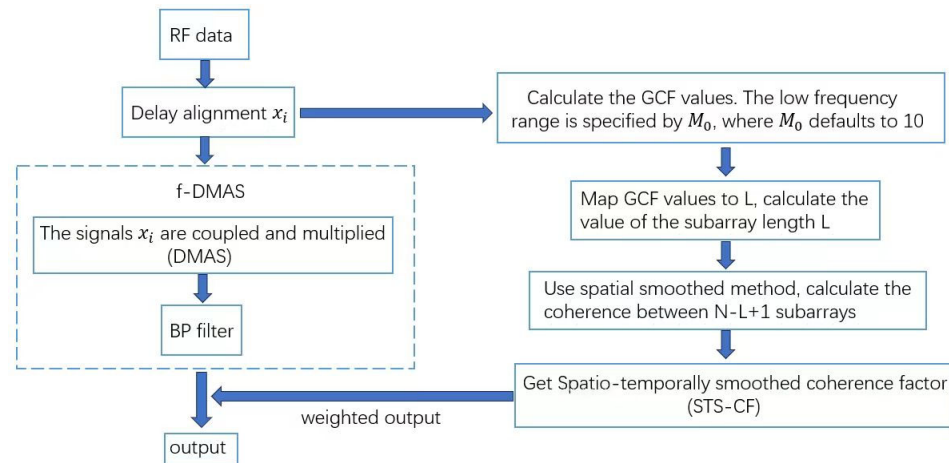


Figure 1. Flow chart of the proposed methods.

The flow of the algorithm is to weigh the output of the DMAS with the GSTS-CF factor. The key point is to calculate the GSTS-CF factor. The calculation process of GSTS-CF is divided into two steps. The first step is to improve the CF using a spatio-temporal smoothing method to obtain the STS-CF factor. The second step is to detect local coherence with the GCF and map the GCF onto the subarray length L so that its value varies adaptively. So first, we divide the array into $N - L + 1$ subarrays, each containing L elements. This is called the spatial smoothed method, and the diagram is shown in Figure 2.

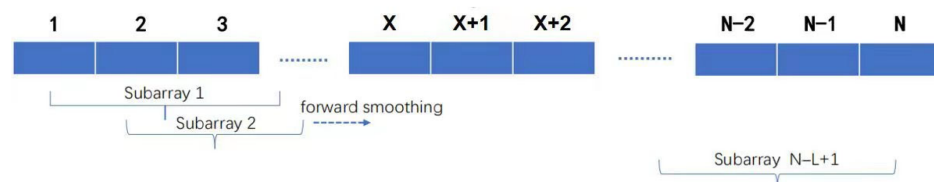


Figure 2. Diagram of the spatial smoothing method.

Figure 2 shows the ultrasonic probe consisting of N array elements. The spatial smoothing method is used to process the data by dividing the N array elements into $N - L + 1$ subarrays, the first subarray contains the 1st to the L th array element, the second subarray contains the 2nd to the $L + 1$ th array element, and so on, and the $N - L + 1$ th

subarray contains the $N - L + 1$ th to the N th array element. The spatial smoothed method computes the coherence of the subarray beamsums instead of computing the coherence with a single element. Equation (1) calculates coherence using a single subarray, while Equation (2) is a spatial smoothed method based on Equation (1), which uses a subarray of L array elements instead of a single array element to calculate the coherence between the arrays. Further, we measure the coherence of the subarrays at $2k + 1$ neighbouring time samples instead of a single time sample, which have improved array gain on SNR and lowered side lobe levels. This is called the spatio-temporally smoothed method. L , as an adjustable parameter, can only be determined empirically. In order to make L adaptively changeable, we use the GCF to detect local coherence and map the GCF to the subarray length L .

In general, as the subarray length increases, the STS-CF approaches 1, thus enhancing robustness at the expense of lateral resolution. Therefore, to maintain the scatter pattern, the L value should be larger, while for echo-free cysts and highly echogenic reflectors, the L value should be smaller to obtain satisfactory image resolution and contrast [16].

Considering the performance of the GCF, the GCF values are small in non-coherent scattering targets (i.e., in echo-free capsules), large in strongly coherent scattering targets (i.e., high-echo reflectors), and tend to be moderate in low-coherent scattering targets (i.e., scattering spots).

According to the analysis above, when the value of GCF is large or small, we want the corresponding L to be small, while when the value of GCF tends to be medium, we want the value of L to be large.

In order to further determine the mapping relationship between GCF and L , we select some points in the incoherent region, strongly coherent region, and low-coherent region, respectively, to calculate the GCF value, and determine the appropriate L value at that point. The evaluation criterion of L -optimal solutions is that in the low coherence region, the scattering variance is the smallest, and in the strongly coherent region and the incoherent region, the lateral resolution is the best. Different echo targets correspond to different GCF values, and we selected 50 different targets whose GCF values were uniformly distributed between 0 and 1. We also calculated the optimal L values corresponding to these 50 targets and plotted a scatter plot, as shown in Figure 3a, using the GCF value of the point as the horizontal coordinate and the L value as the vertical coordinate. The scatter plot is plotted in matlab and then the `geom_smooth()` function is used to fit the scatter points; the optimal model is selected as the Gaussian function model by calculating the AIC value. Thus, the mapping of GCF to L is shown in Equation (5), and the fitting curve is shown in Figure 3b.

$$L(p) = \text{fix} \left[N \times e^{-\left(\frac{\text{GCF}(p)-0.5}{\alpha}\right)^2} \right] \tag{5}$$

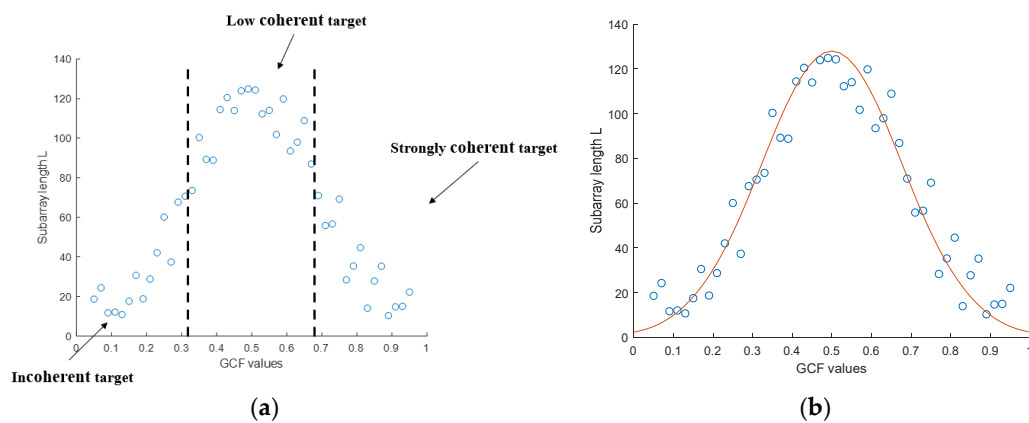


Figure 3. (a) The scatter plot of appropriate L for GCF. (b) Fitting curves for scattered points.

The fix is an integer operation, and $GCF(p)$ is derived from Equation (3), which takes values from 0 to 1, and the range of $L(p)$ is 0 to N . The value of parameter α ranges from 0 to 2. The smaller α is, the faster $L(p)$ changes, and the more sensitive the algorithm is to the detection of the target but the less robust [17]. In this paper, $\alpha = 0.2$. The cutoff frequency M_0 of the low-frequency region in GCF is selected empirically, and different selection will affect the results. In this paper, $M_0 = 10$.

Then, bring $L(p)$ into Equation (2) and replace fixed L with adaptive $L(p)$ to obtain the expression of GSTS-CF at point p :

$$GSTS-CF(p) = \frac{\sum_{k=-K}^K \left| \sum_{l=1}^{M-L(p)+1} \sum_{m=l}^{L(p)+l-1} x_m(p+k) \right|^2}{(M-L(p)+1) \sum_{k=-K}^K \sum_{l=1}^{M-L(p)+1} \left| \sum_{m=l}^{L(p)+l-1} x_m(p+k) \right|^2} \quad (6)$$

The method adaptively changes the subarray length, which gives it a stronger scatter retention capability compared with the conventional CF, but the noise reduction capability is not sufficient, thus combining it with DMAS. Weighting the output of DMAS with GSTS-CF to obtain the output expression of DMAS + GSTS-CF as:

$$y_{DMAS+GSTS-CF} = y_{DMAS} \times GSTS - CF(p) \quad (7)$$

y_{DMAS} is derived from Equation (4).

3. Simulation and Experimental Datasets

3.1. Simulated Data Set

A linear array probe with 128 elements (element width = 0.25 mm, spacing = 0.28 mm, gap = 0.03 mm) was simulated using field ii for the generation of single plane-waves. The excitation was a two-period Hanning-weighted sinusoidal excitation pulse with the central frequency set at 3 MHz. The sampling frequency was 40 MHz. Two experiments were set up in the sound field: the first was scattering points simulation and the second d was a cyst simulation. All are images displayed at a 60 dB dynamic range. The details are as follows.

In the point imaging simulation, four-point pairs are placed evenly at depths of 20 mm to 50 mm. The two points in a point pair are spaced 2 mm apart laterally. This experiment analyzes the lateral resolution of the algorithm by whether the two points in the point pair are clearly visible.

In the cyst simulation, the test model consists of 10,000 points, randomly distributed in a $40 \times 10 \times 5 \text{ mm}^3$ box. Within this volume, the reflectivity has a Gaussian distribution. Embedded in this area is a cylindrical cyst of 3 mm diameter, centrally located at $(x, y, z) = (0, 0, 45) \text{ mm}$. It is assumed that the cyst is echo-free and that the reflection coefficient of its internal scattering points is zero.

3.2. Experimental Data Set

Vivo carotid scanning experiments were carried out using a Heskell 256-channel ultrasound signal collector and RF data before beamforming was acquired using an L-15 (40 MHz) line array probe. The probe emits a single plane-wave during the experiment. The dynamic range of the images was 60 dB [17]. All subjects gave their informed consent for inclusion before they participated in the study. The study was conducted in accordance with the Declaration of Helsinki.

3.3. Image Quality Metrics

In order to quantitatively assess the performance of different beamforming methods, the following metrics are quoted in Section 4: the lateral resolution, contrast ratio (CR), contrast-to-noise ratio (CNR), and speckle SNR (sSNR) [18]. The lateral resolution is measured by calculating the full width at half maximum (FWHM, -6 dB beam width) [19] of the main lobe in a lateral direction. The CNR is used to evaluate whether the image detail

is sufficiently sharp, and sSNR is used to evaluate the quality of background scatter [20]. The CR, CNR, and sSNR are defined as follows:

$$CR = 20 \log_{10} \left(\frac{\mu_i}{\mu_b} \right) \quad (8)$$

$$CNR = \frac{|\mu_i - \mu_b|}{\sqrt{\sigma_b^2 - \sigma_i^2}} \quad (9)$$

$$sSNR = \frac{\mu_b}{\sigma_i} \quad (10)$$

where μ_i and μ_b are the average image intensities (before logarithmic compression) of the cyst and background within a region, while σ_i^2 and σ_b^2 are the corresponding variances.

4. Results

4.1. Simulated Point Target Results

From Figure 3a,b, we can see that the artifacts of DMAS are much smaller than those of DAS, which is due to the fact that the correlation operation brings the metric of backscattered signal coherence into the beamforming process, achieving better spurious and noise rejection, but the image intensity decays as the depth increases [21–23]. The weighted image has a better contrast and resolution, which can be seen in Figure 4c–f. In the four images above, it can be found that the CF-weighted image has the sharpest resolution of point pairs and fewer surrounding artefacts. The method proposed in this paper (GSTS-CF) is the next best, and finally STS-CF is evaluated [14,24].

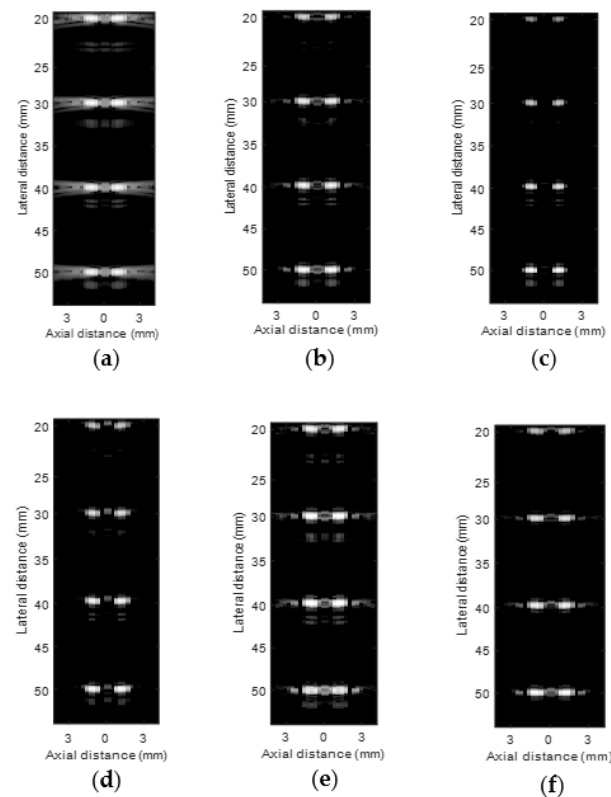


Figure 4. Simulated single plane-wave imaging with a dynamic range of 60 dB. (a) DAS image, (b) DMAS image, (c) DMAS weighted by the CF, (d) DAS weighted by the CF, (e) DMAS weighted by the STS-CF, (f) DMAS weighted by the GSTS-CF. All images are shown in a 60 dB dynamic range.

To further compare the lateral resolution of the different beamformer, we draw the lateral projections of Figure 4 in Figure 5, while calculating the FWHM of the different beamformer based on the lateral projections [25]. From Figure 5, it can be found that the combination of CF and DMAS has the narrowest main lobe width. Weighting DMAS with STS-CF also improves the lateral resolution, but compared to DMAS-CF, there is still a gap. In point imaging, the combination of DMAS and CF gives the best resolution because of less clutter interference and a high echo SNR, but in complex environments with a low SNR, the method will produce a large number of artifacts. The proposed method, which combines the improved GSTS-CF with DMAS, has a slightly worse main lobe width and side lobe amplitude than DMAS-CF, which weakens the suppression effect of CF and makes a compromise between imaging clarity and algorithmic robustness [26]. It can also be seen from Figure 5 that the GSTS-CF has a much-improved lateral resolution compared to the STS-CF, and its FWHM converges to that of the CF-weighted beamformer. Although CF-weighted beamformers have the best lateral resolution, they produce artefacts and uneven background scatter in complex environments, as will be seen in the following experiments.

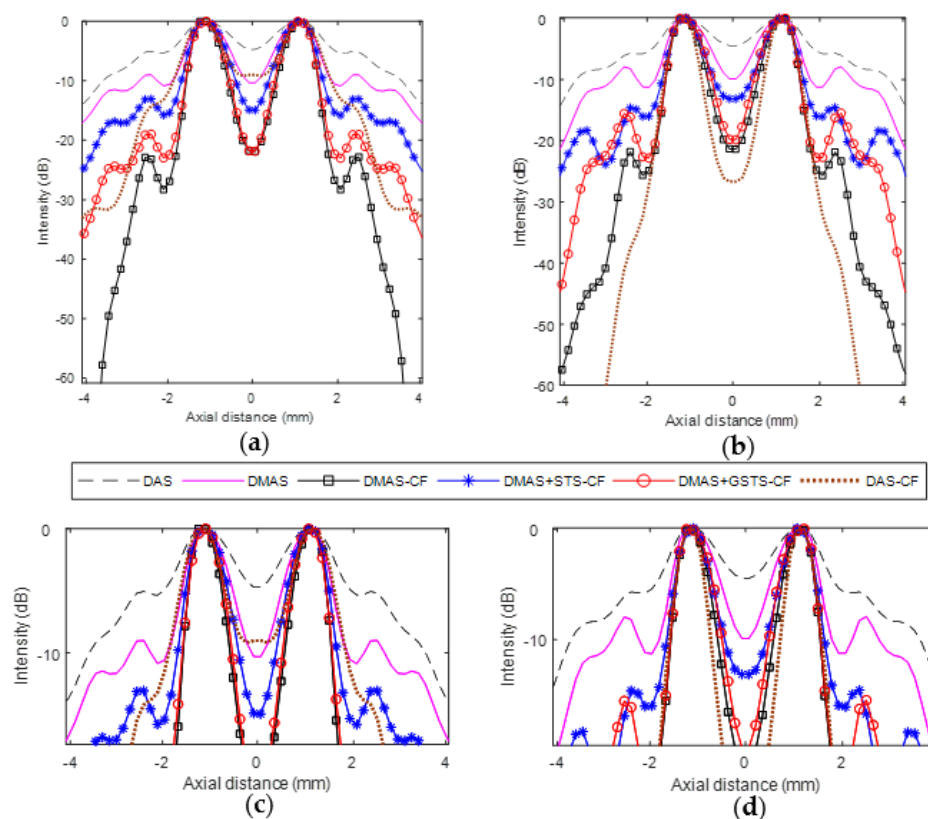


Figure 5. Lateral projections of the single plane-wave images in Figure 4. The point pairs were located at (a) 20 mm and (b) 40 mm. The corresponding zoomed-in figures are shown in (c,d).

From Table 1, we can see the variation in the lateral resolution of different beamformers. The CF-weighted beamformer has a narrower main lobe and higher lateral resolution due to the fact that CF works well in a simple scattering environment with a high signal-to-noise ratio [27]. The combination of GSTS-CF and DMAS achieves a lateral resolution similar to that of the CF-weighted beamformer, which is significantly better than DMAS as well as DMAS + STS-CF.

Table 1. The FWHM for different methods at 20 mm and 40 mm depth.

Method	FWHM (mm)	
	20 mm	40 mm
DAS	3.762	3.831
DMAS	1.032	1.157
DAS-CF	0.525	0.543
DMAS-CF	0.463	0.584
DMAS + STS-CF	0.587	1.034
DMAS + GSTS-CF	0.494	0.612

4.2. Simulated Cyst Target Result

A cyst is synthesized to compare the imaging quality of different algorithms [18]. Figure 6 shows that compared to DAS, DMAS has a clearer cyst demarcation line and lower overall gray value. This is because DMAS has a narrower main lobe and noise floor. Thus, we know that the performance of multiplying and summing is higher than summing, and using adaptive weighting for DMAS can further improve the imaging quality. In Figure 6c,d, the CF over-suppresses the signal. Although the clutter in the cyst was effectively removed, the background region was also over-suppressed, resulting in a lower average level of background intensity (see Table 1) and an increase in background scatter variance, along with a large number of artefacts [19]. It is also seen that the imaging reconstruction in Figure 6c is biased. Because the off-axis signal amplitude is much larger than the true signal amplitude when imaging in the region near the highlighted scatterer, using CF directly would only result in incorrect imaging reconstruction [28]. By making a comparison, we can see that DMAS + STS-CF and DMAS + GSTS-CF have clear cyst demarcation lines, effectively eliminating background region artifacts and suppressing clutter in the cyst region. The method proposed in this paper adaptively evaluates the subarray length with GCF, and it has a more uniform background and lower scatter variance than DMAS + STS-CF [29].

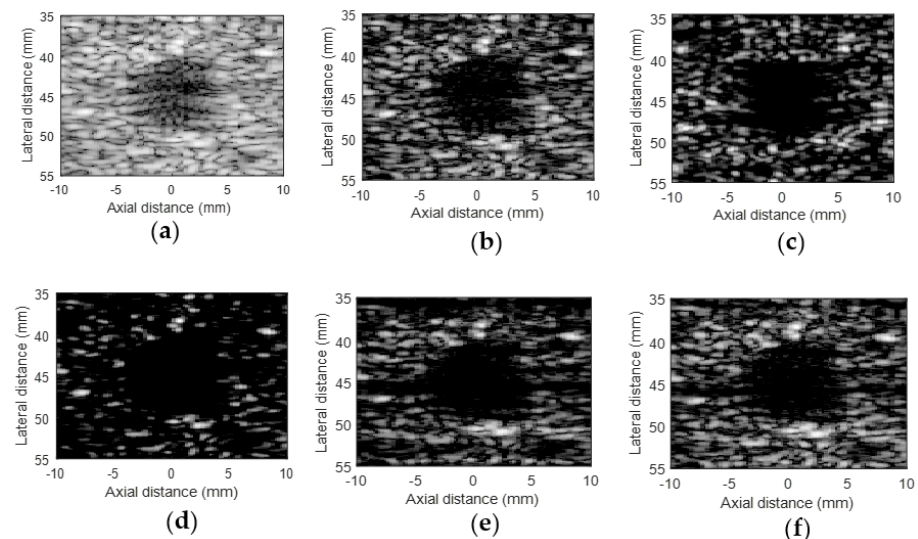


Figure 6. Single plane-wave images of the computer-generated cyst phantom reconstructed using (a) DAS, (b) DMAS, (c) DAS+CF, (d) DMAS + CF, (e) DMAS + STS-CF, (f) DMAS + GSTS-CF. All images are shown in a 60 dB dynamic range.

Lateral cross-sections through the cyst target in the simulated images are shown in Figure 7. It can be seen that DMAS-CF and DMAS + GSTS-CF have the lowest average grey values, indicating that the internal clutter of the cyst is effectively removed [30]. The greatest variation is seen at the cyst demarcation line, indicating that the two methods have the clearest boundaries. Table 2 presents the results of the evaluation of the parameters

σ_b^2 , CR, CNR, and sSNR, and the areas used to calculate these indicators are shown in the rectangle in Figure 6 [31]. It can be seen that DMAS-CF has the highest CR and the lowest CNR and sSNR, while DAS has the lowest CR and the highest CNR and sSNR. This indicates that the normal DAS has the best ability to preserve scatter quality despite its low CR; however, neither method has the best CR, CNR, and sSNR at the same time. The DMAS + GSTS-CF is a compromise between the CR and CNR and sSNR. Its CR is comparable to the DMAS-CF, and CNR and sSNR are comparable to the DAS, while it can be seen that the GSTS-CF outperforms the STS-CF. For σ_b^2 , DMAS + GCTS-CF is also low, just above DAS. This indicates a more uniform background scatter.

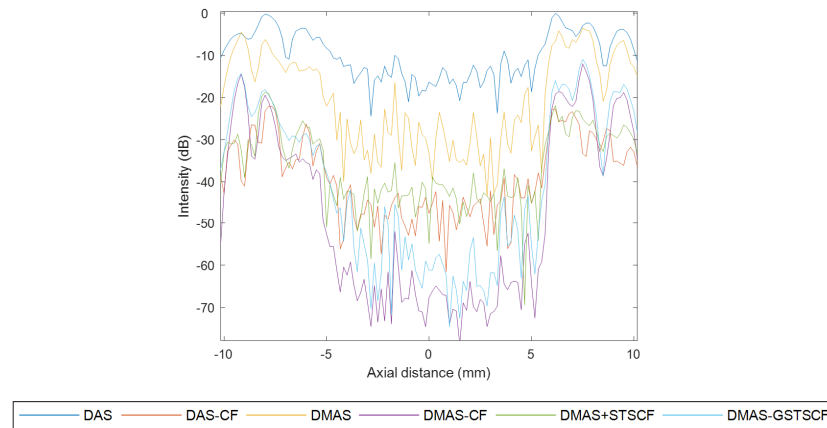


Figure 7. Lateral cross-sections through the cyst target in the simulated images.

Table 2. The cyst average intensity, background average intensity, CR, CNR, and sSNR of cysts for different methods.

Method	μ_i	μ_b	CR (dB)	CNR	sSNR	σ_b^2
DAS	2.3838×10^{-4}	3.60×10^{-3}	-12.7348	1.7998	1.9323	0.0173
DMAS	1.7782×10^{-4}	7.09×10^{-4}	-16.6694	1.2375	1.4648	0.0698
DAS-CF	3.2876×10^{-5}	6.03×10^{-4}	-20.2362	0.9213	1.1923	0.0876
DMAS-CF	4.2484×10^{-7}	3.03×10^{-5}	-32.9846	0.7694	0.9386	0.0945
DMAS + STS-CF	5.9576×10^{-5}	3.09×10^{-4}	-21.6455	1.3393	1.5328	0.0583
DMAS + GSTS-CF	1.1661×10^{-6}	5.03×10^{-4}	-29.3099	1.5420	1.7632	0.0352

4.3. Carotid Artery Experiment

Experiments were performed on human carotid artery scans, and the scanning site and ultrasound signal acquisition device are shown in Figure 8. The RF data were processed using a series of beamforming methods and represented on a 60 dB dynamic range. The model diagram of the imaging site and the final imaging results are shown in Figure 9.

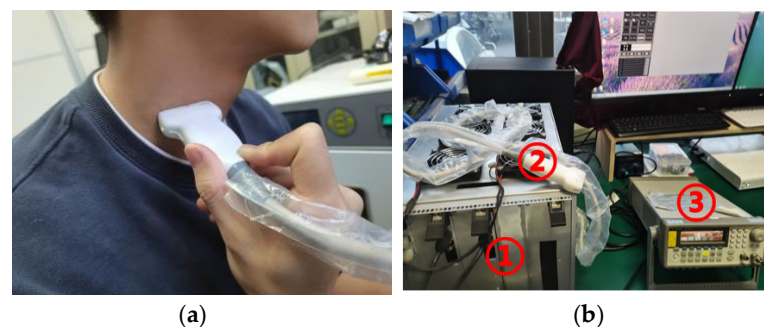


Figure 8. (a) Location of the collected carotid artery data. (b) Ultrasound signal acquisition device. ① RF receiver and transmitter circuits, ② line array probe, ③ signal generator.

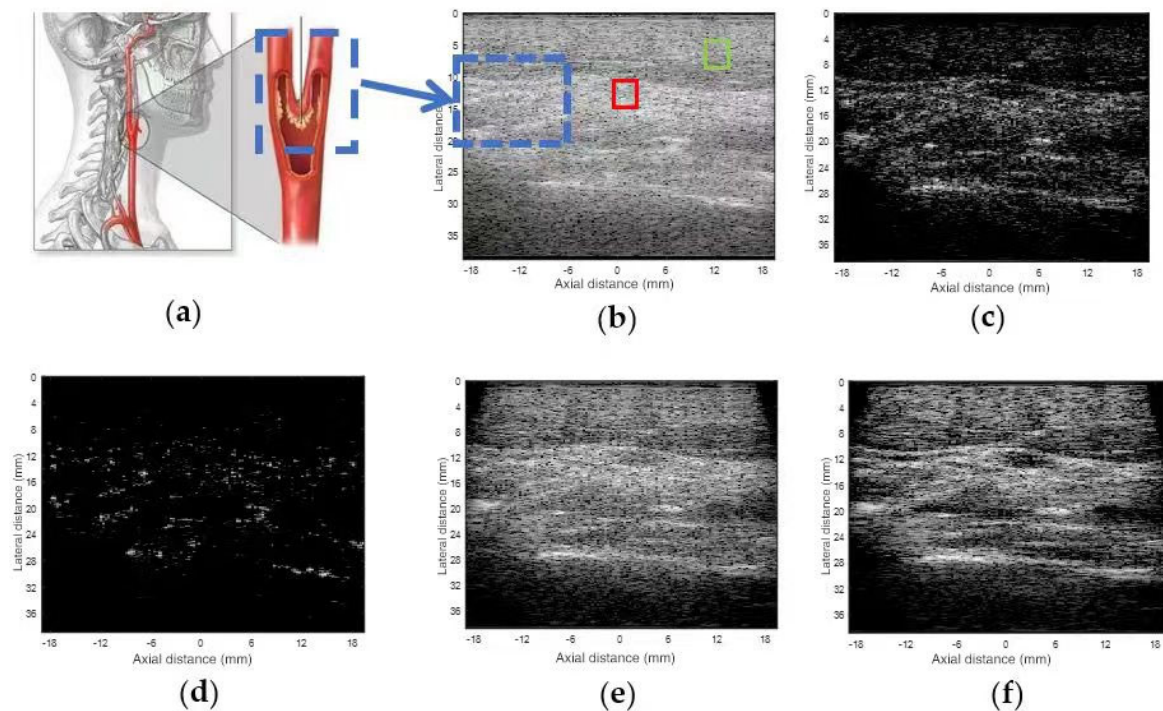


Figure 9. Carotid artery model maps and plane-wave imaging results. The green and red boxes indicate the areas where data μ_i and μ_b were collected (a) Carotid artery model maps, (b) DAS, (c) DMAS, (d) DMAS + CF, (e) DMAS + STS-CF, (f) DMAS + GSTS-CF.

Compared with the simulation, this experimental object has a more complex structure and more noise disturbances. In addition to the coherent noise of the echoes considered in the simulation, there are a series of conditions affecting the signal quality, such as phase distortion caused by the different transmission media and signal distortion caused by the limited performance of the acquisition device. Therefore, to improve the imaging quality of the experiment, we need a more precise signal acquisition device with the assistance of interpolation processing and ultrasonic image denoising technology [32]. Although all of this experimental imaging has some speckle noise, the analysis of the performance of different algorithms is not affected.

It can be seen from Figure 9 that DMAS brings about a higher contrast ratio, but at the same time it results in artifacts in the background, and the overall quality of the image becomes darker. DMAS-CF suppresses the signal excessively, leading to image reconstruction errors, while DMAS + GSTS-CF has a more uniform background area, and the demarcation line between the vessel wall and the lumen can be seen more clearly. At the same time, there are fewer artifacts in the echoless region inside the lumen. Compared to the over-suppression of DMAS + CF, DMAS + GSTS-CF provides higher algorithmic robustness, suppresses artifacts within the vessel lumen, and results in more uniform tissue in the perivascular region. In contrast, although DMAS + STS-CF had similar effects, its performance was lower than that of DMAS + GSTS-CF.

The μ_{lumen} CR, CNR, and sSNR obtained by the different methods are given in Table 3, and the regions used to estimate these metrics are marked with rectangular boxes in Figure 9 (μ_{lumen} is the average value of the vascular lumen region, which reflects the ability of clutter suppression in the vascular lumen). In a complex scattering environment, the CF-weighted beamformer has a very low CNR and sSNR, while the DAS has the lowest CR. The GSTS-CF well balances the CR, CNR, and sSNR, suggesting that the GSTS-CF can preserve scatter patterns well and achieve a high contrast.

Table 3. Average intensity of the carotid lumen and sSNR of the scattered area.

Method	μ_{lumen}	CR	CNR	sSNR	σ_b^2
DAS	7.8059×10^4	-11.324	2.0238	2.9260	1.58
DMAS	4.6285×10^4	-19.736	1.2876	2.0006	2.87
DMAS-CF	3.2523×10^3	-33.254	0.2375	1.5832	5.47
DMAS + STS-CF	3.3379×10^4	-25.232	1.3236	2.4815	2.53
DMAS + GSTS-CF	1.7438×10^4	-28.765	1.6342	2.8156	1.96

5. Discussion

In this paper, we use a coherence factor to improve the performance of DMAS, and our motivation is to achieve a trade-off between lateral resolution and scattering retention performance. Compared with DMAS + CF, the proposed method better preserves the scatter pattern without significantly reducing the lateral resolution. Compared with DAS, the proposed method greatly improves the lateral resolution and contrast while having an approximate background pattern. GSTS-CF is essentially an improved STS-CF who uses GCF as a local coherence detection tool and adaptively selects the appropriate subarray length to conduct spatial smoothing. The combination of GSTS-CF and DMAS further improves the image quality.

Tables 1–3 show that the proposed method improves lateral resolution (20 mm depth) by 86.87% compared to DAS, 52.13% compared to DMAS, 15.84% compared to DMAS + STS-CF, and has a full width at half maxima (FWHM), similar to DMAS-CF. The proposed method improves the speckle signal-to-noise ratio (sSNR) by 87.85% (simulation) and 77.84% (in carotid) compared to DMAS-CF, 20.37% (simulation) and 40.74% (in carotid) compared to DMAS, 15.03% (simulation) and 13.46% (in carotid) compared to DMAS + STS-CF, and has sSNR and scatter variance similar to DAS.

Because the subarray length L for GSTS-CF is estimated by GCF, the performance of the proposed method is influenced by the M_0 (cutoff frequency in the molecule of GCF). As can be seen from Equation (1), the GCF increases with the increase in M_0 , leading to the change in $L(p)$ in Equation (4). From Figure 3, it can be seen that in incoherent target, $L(p)$ increases with the increase in GCF, which leads to a slight decrease in lateral resolution but a more uniform scattering area. In strongly coherent target, $L(p)$ decreases with the increase in GCF, leading to an improvement in the lateral resolution but a decrease in the scattering quality. In low-coherent targets, the change in GCF has little effect on the results because the curve of GCF values mapping to the length of subarray $L(p)$ changes slowly in this region. In clinical applications, we can change the value of M_0 according to different environments, and the default of M_0 in this paper is 10.

During carotid data acquisition, the SNR of the signal is much lower than during cyst simulation, especially when receiving echoes from deeper regions with greater signal attenuation. In Figure 9, the images generated by DMAS + CF may not be suitable for clinical applications because of the significantly lower amplitude levels in the background and the loss of texture information. This is due to the fact that each channel signal has different amounts of correlated noise and interference, and they have different SNRs. Therefore, the weighting factor varies widely, and these artifacts may appear.

DMAS + STS-CF uses the spatio-temporally smoothed method, which enhances the robustness to noise interference and side lobe interference in coherent measurements. As a result, there is a lower scattering variance and higher sSNR, but the lateral resolution is reduced. However, the artifacts of DMAS + STS-CF are more severe in the carotid experiment (Figure 9) than in the cyst simulation (Figure 6). Because the choice of L is fixed, it is necessary to choose a different L for different scenarios in clinical applications, which affects the performance of the algorithm.

In Figure 9f, DMAS + GSTS-CF has higher robustness in complex environments. Compared to DMAS + STS-CF, the method estimates a value of $L(p)$ with GCF at each imaging point, which significantly removes these artifacts by improving the scatter pattern

(lower scatter variance and higher sSNR) while maintaining the clutter rejection capability (lower mean value (μ_{lumen}) in the vessel lumen).

Since the adaptive subarray length is estimated by the GCF, the performance of the proposed method is affected by the cut-off frequency M_0 , and therefore in clinical applications there may be drawbacks, such as noise, clutter, or other types of artefacts, if the parameters are not set correctly. Nevertheless, the proposed method also has potential in clinical applications. This is because the proposed method allows for a flexible selection of the subarray length L according to the echo target and thus improves the lateral resolution along with speckle protection. Thus, it may have potential for applications in the heart, carotid artery, thyroid, tumors, etc. [33–36]. Using the GCF to estimate the subarray length $L(p)$ leads to a significant increase in computational effort because of the large number of Fourier transforms in the GCF. However, graphics processing unit calculations have been used to accelerate these beamformers for real-time imaging and thus can be used in the method proposed in this paper to improve computational efficiency.

6. Conclusions

To improve the speckle quality (lower scatter variance and higher sSNR) without significantly reducing the lateral resolution, we propose an adaptive spatio-temporally smoothed coherence factor called GSTS-CF and combine it with DMAS. The simulation and experimental results show that the method can obtain better background scattering without affecting the lateral resolution. The algorithm is more robust and more suitable for clinical applications.

Author Contributions: In this paper, Z.G. is responsible for methodology and software. X.G. is responsible for data curation and investigation. F.Y. is responsible for visualization, writing—original draft preparation, and validation. Y.Z. is responsible for writing—reviewing and conceptualization. L.L., C.Z. and Y.W. are responsible for supervision and editing. All team members participated in the article work, and there were no conflicts of interest between the teams. All authors have read and agreed to the published version of the manuscript.

Funding: This research was funded by Sichuan Science and Technology Major Project (No.2022ZDZX0033) and the Key Research Pro-gram of the Chinese Academy of Sciences (No. ZDRW-ZS-2021-1).

Data Availability Statement: Data sharing is not applicable to this article.

Conflicts of Interest: There are no conflict of interest among the authors.

References

1. Wells, P.N.T. Ultrasonics in medicine and biology. *Phys. Med. Biol.* **1977**, *22*, 629–669. [[CrossRef](#)] [[PubMed](#)]
2. Tanter, M.; Fink, M. Ultrafast imaging in biomedical ultrasound. *IEEE Trans. Ultrason. Ferroelectr. Freq. Control* **2014**, *61*, 102–119. [[CrossRef](#)] [[PubMed](#)]
3. Montaldo, G.; Tanter, M.; Bercoff, J.; Benech, N.; Fink, M. Coherentplane-wave compounding for very high frame rate ultrasonography and transient elastography. *IEEE Trans. Ultrason. Ferroelectr. Freq. Control* **2009**, *56*, 489–506. [[CrossRef](#)] [[PubMed](#)]
4. Matrone, G.; Savoia, A.S.; Caliano, G.; Magenes, G. The delay multiply and sum beamforming algorithm in ultrasound B-mode medical imaging. *IEEE Trans. Med. Imaging* **2015**, *34*, 940–949. [[CrossRef](#)] [[PubMed](#)]
5. Matrone, G.; Ramalli, A.; Tortoli, P.; Magenes, G. Experimental evaluation of ultrasound higher order harmonic imaging with filtered delay multiply and sum (F-DMAS) non-linear beamforming. *Ultrasonics* **2018**, *86*, 59–68. [[CrossRef](#)] [[PubMed](#)]
6. Synnevåg, J.F.; Austeng, A.; Holm, S. Adaptive beamforming applied to medical ultrasound imaging. *IEEE Trans. Ultrason. Ferroelectr. Freq. Control* **2007**, *54*, 1606–1613. [[CrossRef](#)]
7. Synnevåg, J.F.; Austeng, A.; Holm, S. A low-complexity data-dependent beamformer. *IEEE Trans. Ultrason. Ferroelectr. Freq. Control* **2010**, *57*, 281–289.
8. Hollman, K.W.; Rigby, K.W.; O'donnell, M. Coherence factor of speckle from a multi-row probe. In Proceedings of the 1999 IEEE Ultrasonics Symposium, Tahoe, NV, USA, 17–20 October 1999; pp. 1257–1260.
9. Nilsen, C.I.C.; Holm, S. Wiener beamforming and the coherence factor in ultrasound imaging. *IEEE Trans. Ultrason. Ferroelectr. Freq. Control* **2010**, *57*, 1329–1346. [[CrossRef](#)]

10. Li, P.C.; Li, M.L. Adaptive imaging using the generalized co-herece factor. *IEEE Trans. Ultrason. Ferroelectr. Freq. Control* **2003**, *50*, 128–141.
11. Xu, M.; Yang, X.; Ding, M.; Yuchi, M. Spatio-temporally Smoothed Coherence Factor for Ultrasound Imaging. *IEEE Trans. Ultrason. Ferroelectr. Freq. Control* **2014**, *61*, 182–190. [[CrossRef](#)]
12. Shan, T.J.; Wax, M.; Kailath, T. On spatial smoothing for direction-of-arrival estimation of coherent signals. *IEEE Trans. Acoust. Speech Signal Process.* **1985**, *33*, 806–811. [[CrossRef](#)]
13. Lan, Z.; Jin, L.; Feng, S. Joint Generalized Coherence Factor and Minimum Variance Beamformer for Synthetic Aperture. *IEEE Trans. Ultrason. Ferroelectr. Freq. Control* **2021**, *68*, 1167–1183
14. Varray, F.; Kalkhoran, M.A.; Vray, D. Adaptive minimum variance coupled with sign and phase coherence factors in IQ domain for plane wave beamforming. In Proceedings of the International Ultrasonic Symposium (IUS), Tours, France, 18–21 September 2016; pp. 1–4.
15. Behar, V.; Adam, D.; Friedman, Z. A new method of spatial compounding imaging. *Ultrasonics* **2003**, *41*, 377–384. [[CrossRef](#)] [[PubMed](#)]
16. Wang, Y.; Li, P. SNR-Dependent Coherence-Based Adaptive Imaging for High-Frame-Rate Ultrasonic and Photoacoustic Imaging. *IEEE Trans. Ultrason. Ferroelectr. Freq. Control* **2014**, *61*, 1419–1432. [[CrossRef](#)] [[PubMed](#)]
17. Wu, X.; Gao, Q.; Lu, M. An improved spatio-temporally smoothed coherence factor combined with eigenspace-based minimum variance beamformer for plane-wave imaging in medical ultrasound. In Proceedings of the 2017 IEEE International Ultrasonics Symposium (IUS), Washington, DC, USA, 6–9 September 2017.
18. Wagner, R.F.; Insana, M.F.; Smith, S.W. Fundamental correlation lengths of coherent speckle in medical ultrasonic images. *IEEE Trans. Ultrason. Ferroelectr. Freq. Control* **1988**, *35*, 34–44. [[CrossRef](#)] [[PubMed](#)]
19. Synnevåg, J.F.; Nilsen, C.I.C.; Holm, S. P2B-13 Speckle statistics in adaptive beamforming. In Proceedings of the 2007 IEEE Ultrasonics Symposium, New York, NY, USA, 28–31 October 2007; pp. 1545–1548.
20. Matone, G.; Ramalli, A.; D’hooge, J. Spatial Coherence Based Beamforming in Multi-Line Transmit Echocardiography. In Proceedings of the 2018 IEEE International Ultrasonics Symposium (IUS), Kobe, Japan, 22–25 October 2018. [[CrossRef](#)]
21. Synnevåg, J.-F.; Austeng, A.; Holm, S. A low-complexity data dependent beamformer. *IEEE Trans. Ultrason. Ferroelectr. Freq. Control* **2011**, *58*, 281–289. [[CrossRef](#)] [[PubMed](#)]
22. Synnevåg, J.-F.; Austeng, A.; Holm, S. Benefits of minimum variance beamforming in medical ultrasound imaging. *IEEE Trans. Ultrason. Ferroelectr. Freq. Control* **2009**, *56*, 1868–1879. [[CrossRef](#)]
23. Zimbico, J.; Granado, D.W.; Schneider, F.K.; Maia, J.M.; Assef, A.A.; Schiefler, N., Jr.; Costa, E.T. Eigenspace generalized sidelobe canceller combined with SNR dependent coherence factor for plane wave imaging. *Biomed. Eng. Online* **2018**, *17*, 109. [[CrossRef](#)]
24. Asl, B.M.; Mahloojifar, A. Minimum variance beamforming combined with adaptive coherence weighting applied to medical ultrasound imaging. *IEEE Trans. Ultrason. Ferroelectr. Freq. Control* **2009**, *56*, 1923–1931. [[CrossRef](#)]
25. Zhao, J.; Wang, Y.; Yu, J.; Guo, W.; Li, T.; Zheng, Y.-P. Subarray coherence based postfilter for eigenspace based minimum variance beamformer in ultrasound plane-wave imaging. *Ultrasonics* **2016**, *65*, 23–33. [[CrossRef](#)]
26. Deylami, A.M.; Jensen, J.A.; Asl, B.M. An improved minimum variance beamforming applied to plane-wave imaging in medical ultrasound. In Proceedings of the 2016 IEEE International Ultrasonics Symposium (IUS), Tours, France, 18–21 September 2016; pp. 1–4.
27. Qi, Y.; Wang, Y.; Yu, J.; Guo, Y. 2-D Minimum Variance Based Plane Wave Compounding with Generalized Coherence Factor in Ultrafast Ultrasound Imaging. *Sensors* **2018**, *18*, 4099. [[CrossRef](#)] [[PubMed](#)]
28. Asl, B.M.; Mahloojifar, A. Contrast enhancement and robustness improvement of adaptive ultrasound imaging using forward-backward minimum variance beamforming. *IEEE Trans. Ultrason. Ferroelectr. Freq. Control* **2011**, *58*, 858–867. [[CrossRef](#)] [[PubMed](#)]
29. Zhang, C.; Geng, X.; Yao, F.; Liu, L.; Guo, Z.; Zhang, Y.; Wang, Y. The Ultrasound Signal Processing Based on High-Performance CORDIC Algorithm and Radial Artery Imaging Implementation. *Appl. Sci.* **2023**, *13*, 5664. [[CrossRef](#)]
30. Ali, I.; Saleem, M.T. Spatiotemporal Dynamics of Reaction–Diffusion System and Its Application to Turing Pattern Formation in a Gray–Scott Model. *Mathematics* **2023**, *11*, 1459. [[CrossRef](#)]
31. Kaddoura, T.; Zemp, R.J. Hadamard Aperiodic Interval Codes for Parallel-Transmission 2D and 3D Synthetic Aperture Ultrasound Imaging. *Appl. Sci.* **2022**, *12*, 4917. [[CrossRef](#)]
32. Khan, S.U.; Ali, I. Application of Legendre spectral-collocation method to delay differential and stochastic delay differential equation. *AIP Adv.* **2018**, *8*, 035301. [[CrossRef](#)]
33. Rindal, O.M.H.; Aakhus, S.; Holm, S.; Austeng, A. Hypothesis of improved visualization of microstructures in the interventricular septum with ultrasound and adaptive beamforming. *Ultrasound Med. Biol.* **2017**, *43*, 2494–2499. Available online: <http://www.sciencedirect.com/science/article/pii/S0301562917302466> (accessed on 5 May 2018). [[CrossRef](#)]
34. Nguyen, N.Q.; Prager, R.W. Minimum variance approaches to ultrasound pixel-based beamforming. *IEEE Trans. Med. Imaging* **2017**, *36*, 374–384. [[CrossRef](#)]

35. Qi, Y.; Wang, Y.; Guo, W. Joint subarray coherence and minimum variance beamformer for multitransmission ultrasound imaging modalities. *IEEE Trans. Ultrason. Ferroelectr. Freq. Control* **2018**, *65*, 1600–1617. [[CrossRef](#)]
36. Szasz, T.; Basarab, A.; Kouame, D. Beamforming through regularized inverse problems in ultrasound medical imaging. *IEEE Trans. Ultrason. Ferroelectr. Freq. Control* **2016**, *63*, 2031–2044. [[CrossRef](#)]

Disclaimer/Publisher’s Note: The statements, opinions and data contained in all publications are solely those of the individual author(s) and contributor(s) and not of MDPI and/or the editor(s). MDPI and/or the editor(s) disclaim responsibility for any injury to people or property resulting from any ideas, methods, instructions or products referred to in the content.